



Numerical Investigations into the Origin of Tip Unsteadiness in a Transonic Compressor

G. An, Y. Wu[†], J. Lang, Z. Chen and B. Wang

*Northwestern Polytechnical University, Xi'an, Shaanxi, 710129, China
Shaanxi Key Laboratory of Internal Aerodynamics in Aero-Engine, China*

[†]Corresponding Author Email: wyh@nwpu.edu.cn

(Received June 6, 2017; accepted February 3, 2018)

ABSTRACT

Three-dimensional numerical simulations are conducted to investigate the origin of flow unsteadiness and its associated unsteady flow phenomena in a transonic compressor rotor. The predicted results are compared with the available experimental data and a good agreement is achieved. The numerical monitoring results and further analyses of the flow field indicate that flow unsteadiness is detected in the passage with the operating condition approaching the stability limit, and the highest oscillating region is at the leading edge of the blade pressure surface; the tip leakage vortex breakdown is not a decisive factor for the flow unsteadiness, and the shock oscillation is a unsteady flow phenomenon resulted from the vibration of the recirculation region; a U-type vortex emerges in the tip leakage vortex breakdown region, and its periodic impingement on the pressure surface of the adjacent blade is treated as a trigger that leads to the flow unsteadiness.

Keywords: Transonic compressor rotor; Flow unsteadiness; Vortex breakdown; Shock wave oscillation.

NOMENCLATURE

A_m	amplitude of massflow oscillation	S	entropy
A_p	amplitude of static pressure oscillation	t	time instant
BPF	blade passing frequency	TAV	Time Average
CAL	calculation	TLV	Tip Leakage Vortex
C_{ax}	axial chord of blade at tip	T_{ref}	reference period
C_p	static pressure coefficient $C_p = \frac{P_s - P_{ref}}{0.5 * \rho U_t^2}$	Vol	volume of recirculation region
f	frequency	U_t	blade tip speed
H_n	normalized helicity $H_n = \frac{\xi^* w}{ \xi^* w }$	V_t	absolute tangential velocity
l_0	chord length	ξ_n	normalized absolute vorticity, $\xi_n = \frac{ \xi }{2\omega}$
P	static pressure	τ	physical time step
ΔP	pressure difference $\Delta P = \frac{P_p - P_s}{0.5 * \rho U_t^2}$	ω	rotor angular velocity
Q	flow rate	Ω_r	radial component of the vorticity

1. INTRODUCTION

Tip leakage flow as an important component of the tip flow field has profound effects on both performance and stability of axial compressors. In a primary study, numerical simulation of the flow

field with four different tip clearances has been carried out on Rotor 67 by Adamczyk *et al.* (1993) and the results indicated that both the efficiency and the pressure ratio were improved with the decrease of the tip clearance. Thus, in order to improve the performance and reliability of compressors, it is essential to have a better understanding of details of

the tip leakage flow structures. With the continuous improvement of experimental methods and development of CFD techniques, causal links between the tip leakage flow and the tip flow unsteadiness in compressors have been substantiated, and researchers have made tremendous progress on these topics.

In the light of prior research, tip flow unsteadiness can be attributed to the following factors,

1) The tip leakage vortex (TLV) breakdown. In the experiments on a low speed axial flow compressor, [Inoue and Kuroumaru \(1986, 1989\)](#) found the unsteady flow phenomenon at near stall operating condition. Based on these experimental observations, [Furukawa *et al.* \(1999, 2000\)](#) conducted a series of numerical simulations in further detail. They pointed out that the TLV breakdown occurred at near stall condition and that the cyclic variations of the flow field were caused by the breakdown of the TLV. [Yamada *et al.* \(2004\)](#)'s single passage simulation on Rotor 37 indicated that the TLV breakdown occurred at near stall condition likewise and there existed a characteristic frequency corresponding to 60% blade passing frequency(BPF).

2) The oscillation of the shock wave and the interaction between the shock and TLV. [Hah *et al.* \(2004\)](#) found that the TLV did not break down even for a rotor operating in the stalled condition through detailed numerical investigation on a swept transonic compressor. They deemed that it was the shock oscillation that gave rise to the flow unsteadiness. Then [Bergner *et al.* \(2006\)](#) presented a different viewpoint that the interaction between the TLV and the shock wave was responsible for the unsteady flow oscillation in the tip flow region after they carried out experimental research on the same compressor rotor.

3) The formation and development of the tip secondary vortex(TSV). Numerical simulation and experiments have been conducted on a single subsonic rotor by [Wu *et al.* \(2010, 2012\)](#). The research showed that TLV breakdown on the near stall condition and a tip secondary vortex originated from the interaction between the main flow and the tip leakage flow. She suggested that the development of the TSV contributed to the oscillation of the efficiency and pressure ratio of the compressor.

4) The oscillation of the tip leakage flow and its interaction with the main flow. [Deng \(2006\)](#) studied the tip leakage flow in a subsonic compressor and noted that static pressure fluctuations induced by tip leakage flow at a relatively low mass flow rate and a large tip clearance might lead to the periodic unsteadiness of the tip clearance flow. He suggested that this unsteady flow phenomenon was a result of dynamic balance between the aerodynamic loading of the blades and the tip leakage flow. [Du *et al.* \(2008\)](#) conducted simulations on Rotor 67, they proposed that the interaction between tip leakage flow and the main flow was considered as key flow structures contributing to the flow unsteadiness.

In the light of the research above, it is clear that

various unsteady flow phenomena were observed in the tip region. However, reasons for the occurrence of the flow unsteadiness are varied due to the difference in research objects. In this paper, unsteady flow phenomena mentioned above will be discussed in order to explore the roles that these complicated flow mechanisms played as the operating condition approached the stability limit, meanwhile, the key factor that contributes to the flow unsteadiness in the rotor passage will be revealed through further analyses of the flow field.

2. TRANSONIC COMPRESSOR ROTOR

A transonic axial compressor rotor, NASA Rotor 35 is used for the present work. The rotor was originally designed as an inlet rotor for a core compressor and tested at NASA Lewis Research Center with a design speed of 17188.17 RPM. The rotor has 36 blades, an inlet tip radius of 25.4 cm, a hub-tip radius ratio of 0.70, an aspect ratio of 1.19, a tip solidity of 1.3, and an axial chord of 2.72 cm at the tip and 4.12 cm at the hub. The compressor is designed for axial inlet flow, and inlet relative velocity is 454.456m/s at the tip at the design speed. Detailed design parameters can be found in [Reid and Moore \(1978\)](#). Experimental data and the time-averaged flow field were acquired by [Van Zante *et al.* \(2000\)](#) using pneumatic probes and a Laser Doppler Velocimetry system, which can be used to validate the numerical simulations.

[Wu *et al.* \(2016\)](#)'s single passage simulation on Rotor 35 has shown that flow unsteadiness was found in tip region at near stall condition, which paves the way for this paper.

3. NUMERICAL METHODOLOGY

3.1 Numerical Scheme

The present simulations are performed with the commercial flow solver EURANUS, which is developed by NUMECA. The three-dimensional Reynolds-averaged Navier-Stokes equations are discretized in space using a cell-centered finite volume formulation. A second-order upwind scheme based on a flux difference splitting formulation is chosen to evaluate the inviscid fluxes so as to capture the TLV sharply near the end-wall. The viscous fluxes are determined in a central differencing manner with Gauss's theorem. An explicit Runge-Kutta scheme with local time step is used to obtain the steady solutions, while the time-accurate solutions are obtained by an implicit dual time-stepping method proposed by [Jameson \(1991\)](#). The Low-Reynold number k-epsilon turbulence model is chosen to estimate the eddy viscosity. The physical time step for time-accurate simulations is determined by rotational speed, and it takes a rotor blade 50 time steps to pass through one pitch (1.93925e-6s for each time step). Within each physical time step, 50 pseudo time iterations are performed. It has been proven that the time step setup is sufficient to capture the details of the flow field.

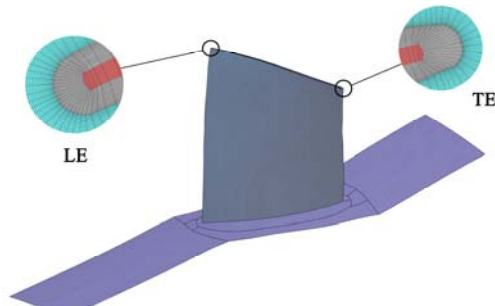


Fig. 1. Computational domain and grid

3.2 Computational Grid

The computational grid for the present simulations is shown in Fig. 1. The blade-passage domain is divided into two zones: the main flow region and the tip flow region. In the light of Van Zante *et al.* (2000)'s investigation, grids near the casing are refined so as to achieve accurate numerical simulation of tip clearance flow. The minimum grid spacing gives $y^+ < 1$ at the walls. Three sets of grids of different densities (1.5×10^6 , 2.4×10^6 , 3.3×10^6) are tested, and it has been proven that the second set (2.4×10^6 cells) is sufficient for the computation. The main flow region is subdivided into 7 grid blocks: An O-type grid is generated around the blade with 53 cells in the pitchwise direction, 97 cells in the spanwise direction and 217 cells in the streamwise direction; The others are all H-type grids. According to the number sequence in Fig. 2(a), they consist of $61 \times 97 \times 37$, $61 \times 97 \times 53$, $61 \times 97 \times 37$, $17 \times 97 \times 17$, $17 \times 97 \times 17$, and $17 \times 97 \times 127$ cells in the pitchwise, spanwise, and streamwise directions, respectively. Butterfly topology is used to model the true tip gap. A H-type grid is generated in the inner zone, which consisted of 25 cells in the pitchwise direction, 37 cells in the spanwise direction, and 127 cells in the streamwise direction, while an O-type grid is generated in the outer zone, which consist of $25 \times 37 \times 127$ cells in the pitchwise, spanwise, and streamwise directions, respectively.

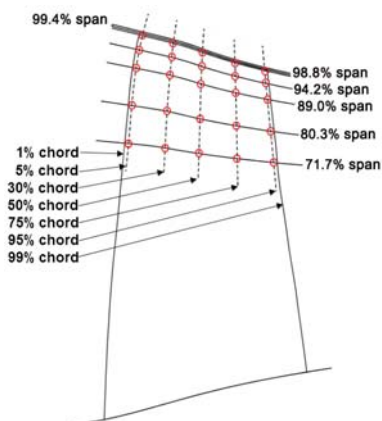


Fig. 2. A schematic view of the arrangement for numerical probes

3.3 Arrangement Scheme for Numerical Probes

Figure 2 shows a schematic view of the

arrangement for numerical probes. Previous studies on this rotor conducted by Wu *et al.* (2016) showed that the most prominent unsteady region was located on the pressure surface of the blade tip. Therefore, numerical probes are only arranged at the pressure surface and above 70% of blade span. As is shown in this figure, the spanwise locations for 10 probes were 99.4%, 98.8%, 94.2%, 89.0%, 80.3%, and 71.7% of blade span respectively. With the axial coordinate of tip leading edge chosen as reference datum, the axial locations for nine probes were 1%, 5%, 10%, 20%, 30%, 50%, 75%, 90%, 99% of C_{ax} .

3.4 Boundary Conditions

No-slip and adiabatic conditions are imposed at solid boundaries. The flow is assumed to be steady-state both at the inlet and outlet of the rotor. The flow angle, total pressure and total temperature are specified to be uniform across the whole inlet domain according to the experimental data and the averaged static pressure is set at the outlet of computational domain.

4. RESULTS AND DISCUSSIONS

4.1 Validation of Numerical Simulation

Figure 3 shows the comparison between the predicted and measured total pressure ratio curves at design speed. As can be seen, the unsteady predicted total pressure ratio curve matches the experimental one well, but it is slightly above the experimental results (about 0.6%) as stall limit approaches. The difference between predicted and experimental mass flow rate at stall limit is 0.164kg/s, while the measurement uncertainties in the experiment conducted by Van Zante *et al.* (2000) is ± 0.3 kg/s. Thus, the mass flow rate difference is in a reasonable range. In addition, colored ovals shown in Fig. 3 represent the variations of total pressure ratio versus time. As can be seen, the total pressure ratio fluctuates over time at operating conditions from U5 to U8.

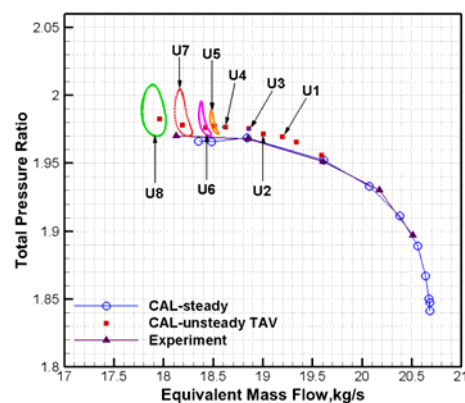


Fig. 3. Total pressure ratio characteristics

In Fig. 4, the absolute tangential velocity distributions on cross channels at 33%, 53%, 72%, 92% rotor chord are compared between numerical and experimental results at peak-efficiency

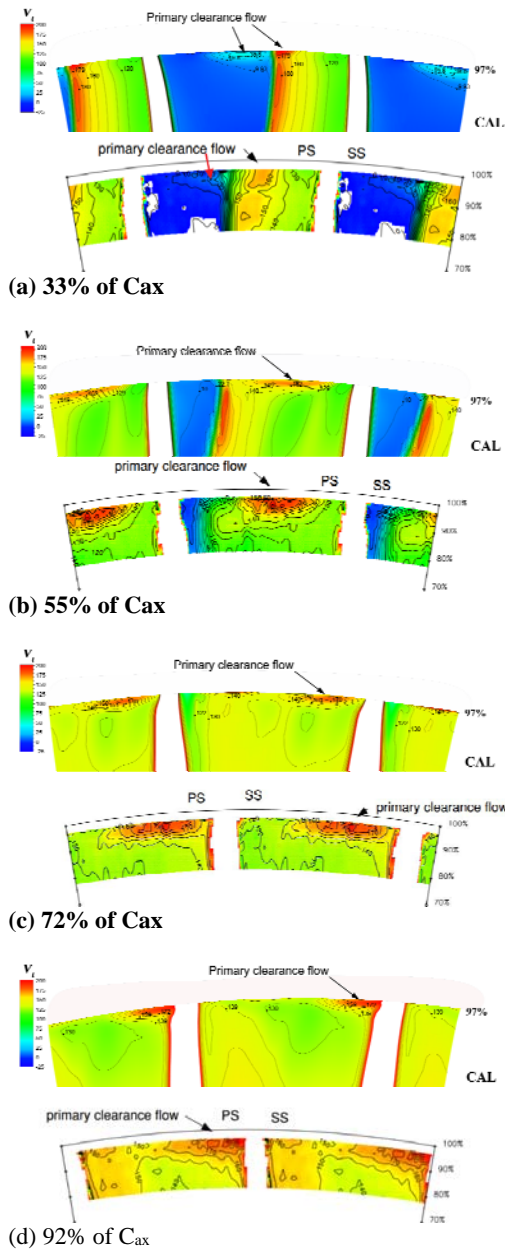


Fig. 4. Measured (Van Zante *et al.*, 2000) and predicted tangential velocity distributions on cross channels at peak-efficiency condition

condition. It is found that, relatively high velocity regions which represent primary clearance flow are well predicted at each axial location. Moreover, the values of tangential velocity associated with the primary clearance flow match with the experiments well. It should be noted that in fact there are two tip leakage flow regions that can be observed in Fig. 4-a. As can be seen in Fig. 5, they appear before and after the shock wave.

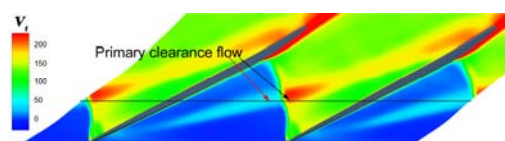


Fig. 5. Contour plots of absolute tangential velocity on the 97% span stream surface for U10

On the whole, the results presented above show that the current simulations produce a satisfactory comparison with available measurement data, thus providing confidence in further analysis of the computed flow fields.

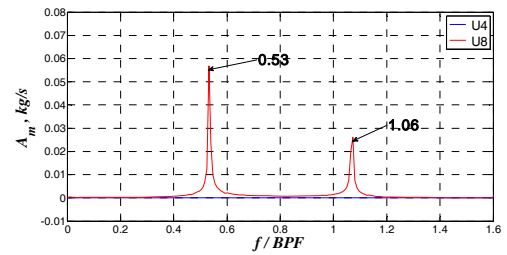
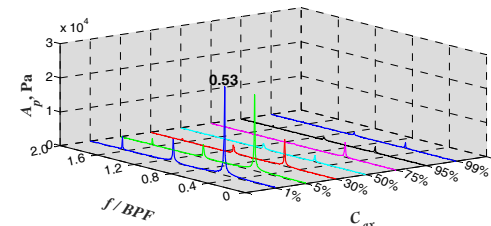


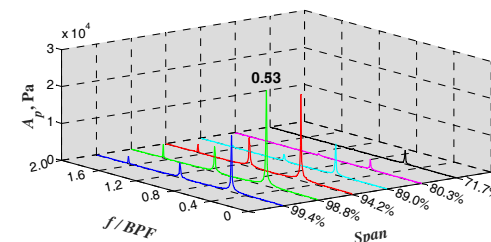
Fig. 6. FFT results of outlet massflow under U4 and U8 conditions

4.2 Analyses of Monitoring Results of Numerical Probes

Figure 6 shows FFT results of outlet massflow under U4 and U8 conditions. Two oscillating frequency components are observed at U8 condition: the dominating frequency component is 0.53 BPF, and the other frequency component is its higher harmonic. Besides, the outlet massflow does not show any oscillation at U4 condition, which agrees with the information shown in Fig. 3.



(a) Probes at 98.8% span



(b) Probes at 1% Cax

Fig. 7. FFT results of static pressure under U8 condition

Figure 7 presents FFT results of static pressure under U8 condition. The results show that the pressure oscillation is detected in the whole passage and that the maximum amplitude of the pressure oscillations appears at 98.8% span, 1% C_{ax} . Besides, the frequency of the pressure oscillation presented in Fig. 7 corresponds to the frequency of the outlet massflow oscillation shown in Fig. 6. This means that the outlet massflow oscillation is originating from the tip flow unsteadiness. Thus, it is reasonable to investigate the origin of flow unsteadiness through analyzing the flow characteristics near the leading edge of the blade tip region.

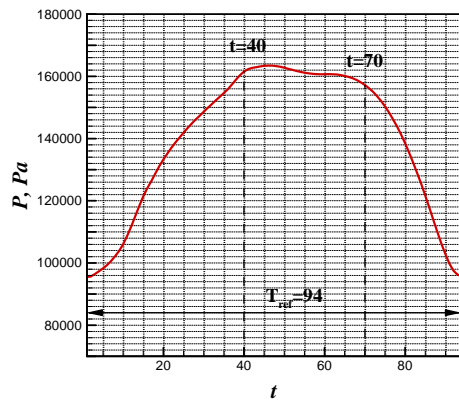


Fig. 8. Variation of static pressure of the numerical probe at 1% C_{ax} , 98.8% span at U8 condition

The frequency of tip flow unsteadiness at U8 condition is 0.53BPF, and its corresponding period is 94τ . In the following, for the convenience of analyses, the reference period T_{ref} at U8 condition is designated as 94τ with its starting at a moment approximate to the minimum value of local static pressure at 1% C_{ax} and 98.8% span on the pressure surface as is shown in Fig. 8. In this figure, it is observed that at first the static pressure increases gradually and reach the highest point at $t=40$, then it experiences a slight decrease from $t=40$ to $t=70$, finally it decreases rapidly and bottoms out at $t=94$.

4.3 Vortex Breakdown

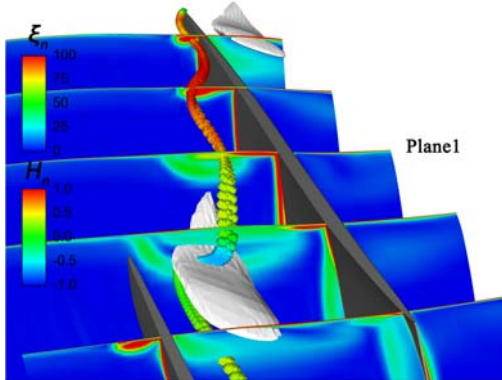


Fig. 9. Normalized absolute vorticity distribution on crossflow planes at U8 condition

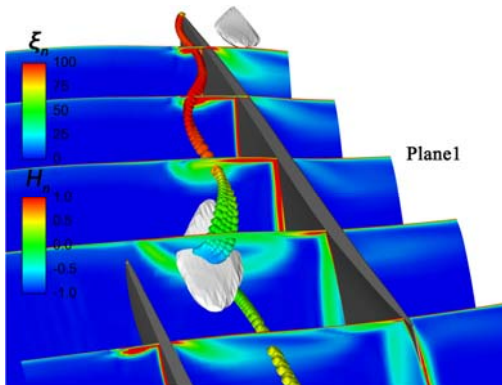


Fig. 10. Normalized absolute vorticity distribution on crossflow planes at U4 condition
Figure 9 provides normalized absolute vorticity

distribution on crossflow planes in a time-averaged flow field at U8 condition. Note that these planes are nearly perpendicular to the trajectory of TLV. Streamlines which flow through the TLV core are colored with normalized helicity. Additionally, reverse flow region identified by the iso-volume with relative tangential velocity less than -1m/s is also shown in this figure. It is found that the TLV has a concentrated absolute vorticity region upstream of the shock wave. However, after the TLV interacts with the shock wave at plane 1, its core region experiences a sudden expansion, and the concentrated absolute vorticity region disappears. In addition, a recirculation region is observed downstream of the shock wave. The flow characteristics mentioned above: a sudden expansion of the vortex core, the disappearance of the concentrated absolute vorticity region, and the appearance of the recirculation region downstream of the shock wave, imply the tip vortex breakdown occurs at this condition according to the numerical investigation results achieved by Leibovich (1978), Deley (1994).

In order to discern whether the breakdown of the TLV is the main cause of the flow unsteadiness, Fig. 10 is shown to provide the normalized absolute vorticity distribution at U4 condition. Based on above discussions, it is known that no characteristic frequencies are detected at this condition. However, the TLV still breaks down at U4 condition according to the information shown in Fig. 10. Thus, it is clear that the TLV breakdown is not a decisive factor for the flow unsteadiness.

4.4 Shock Wave Oscillation

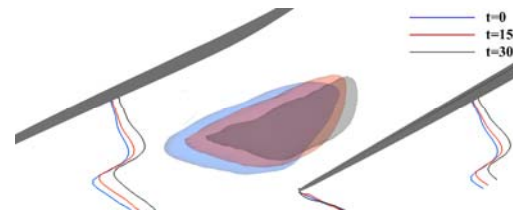


Fig. 11. Locations of the shock wave and the recirculation region at three different time instants

Figure 11 shows locations of the shock wave and the recirculation region at three different time instants. It is found that the shock wave identified by colored lines oscillates with time. Besides, the volume of the recirculation region also varies with time.

In order to explore the reason for the shock oscillation, Fig. 12 provides information about locations of the TLV breakdown point and the shock wave during one T_{ref} . The location of the shock wave is defined as follows: the distance from the shock and TLV intersection point to the leading edge of the blade. The location of the TLV breakdown is defined as follows: the distance from the stagnation point in the vortex core to the leading edge of the blade. Both of these two variables are normalized by the axial chord. It is observed that the vortex breakdown point is located downstream

of the shock wave and that there is a positive correlation between the location of the shock and the TLV breakdown point. In combination with the information given in Fig. 11, we can give an explanation for the shock oscillation: the passage shock can be treated as a detached shock in front of the recirculation region, and the movement of the recirculation region is the driving force of the shock oscillation. As the recirculation region moves upstream, the detached shock will be pushed upstream, and vice versa. Thus, it is known that the location of the shock is closely related to the TLV breakdown. On the one hand, the TLV breakdown is caused by the effect of a strong adverse pressure gradient of the shock. On the other hand, the shock oscillates in the passage due to the movement of the recirculation region which is formed in the vortex breakdown region. Furthermore, it is also found in Fig. 12 that both the shock and the vortex breakdown point move periodically in the passage, and their corresponding period are all 94τ which agrees with the characteristic frequency detected in the flow field. Thus, it can be seen that the movements of the shock and the vortex breakdown point are inextricably bound up with the flow unsteadiness.

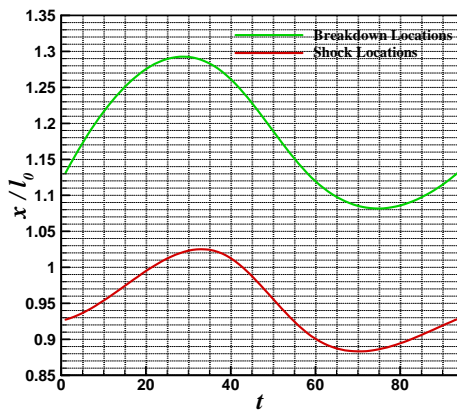


Fig. 12. Locations of the TLV breakdown point and the shock wave during one T_{ref}

In order to clarify the flow mechanisms of these two unsteady flow phenomena, Fig. 13 shows a comparison between the flow rate within the fore 30% of tip chord and the volume of recirculation region. The curves demonstrate that there is a negative correlation between the static pressure and the volume of the recirculation region: when the static pressure rises, the volume of recirculation region will decrease and vice versa. A previous study on vortex breakdown conducted by [Sarpkaya \(1971\)](#) showed that when the upstream swirl was increased, the recirculation region shrank and vice versa. In the light of this conclusion, the periodic oscillation of the recirculation region can be explained as follows: when the leakage flow rate rises, the upstream swirl increases, resulting in a shrink of the recirculation region and vice versa.

Based on the analyses above, it is clear that the expansion and shrink of the recirculation region is the main cause of the shock oscillation and that the

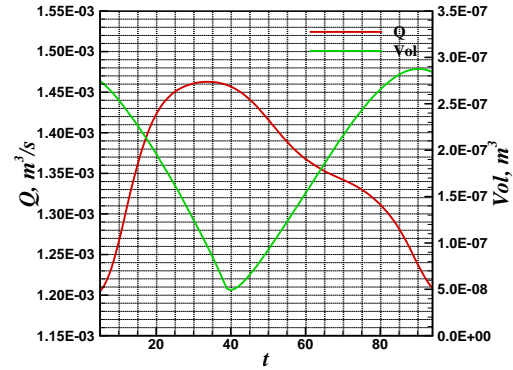


Fig. 13. A comparison between the flow rate within the fore 30% of tip chord and the volume of recirculation region

volume of the recirculation region is dominated by the leakage flow rate. Meanwhile, it is well accepted that the leakage flow rate has direct relevance to the blade loading. Figure 14 presents variation of pressure difference at tip at U8 condition, the pressure difference is normalized by the dynamic pressure based on the rotor tip speed. It is observed that the pressure difference increases gradually from $t=0$, and reaches the highest point at $t=40$, then it falls back. The whole process is consistent with the vibration of the leakage flow rate shown in Fig. 13. Thus, it is known that the vibration of the blade loading is the key factor that leads to the shock oscillation.

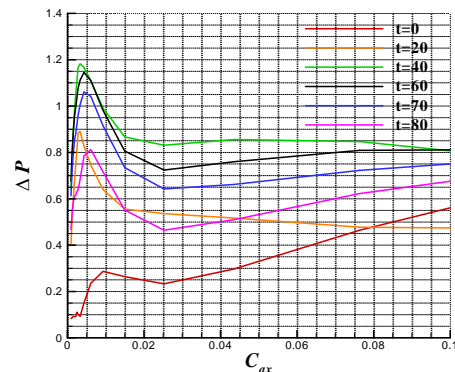


Fig. 14. Variation of pressure difference at tip at U8 condition

4.5 Analyses of Flow Characteristics at Tip Region

In this section, details of the tip flow field are further interrogated to shed light on the flow mechanism by which the tip flow unsteadiness appears.

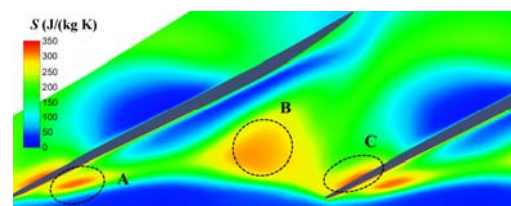


Fig. 15. Time- averaged entropy distribution at 98% span at U8 condition

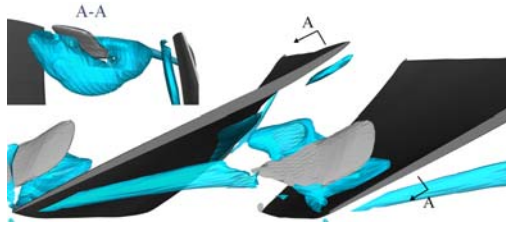


Fig. 16. Illustration of vortices extracted by Lambda 2 method at tip region

Figure 15 shows the time-averaged entropy distribution at 98% span at U8 condition. Three high-entropy regions (A, B and C) are observed in this figure, among which region A is resulted from the TLV. In order to explicit the origin of region B and C, Fig. 16 provides illustration of vortices extracted by Lambda 2 method at tip region. It is observed that besides the TLV there exists a U-type vortex in the middle of the passage. Obviously, high-entropy region B and C are induced by this U-type vortex. Duo to the fact that the U-type vortex encloses the recirculation region, it can be inferred that the origin of the U-type vortex is closely associated with the TLV breakdown.

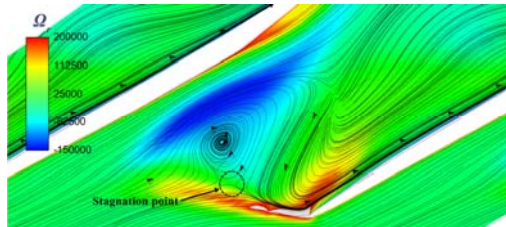


Fig. 17. Time-averaged radial vorticity and streamline distributions at 98% span at U8 condition

Figure 17 shows the time-averaged radial vorticity and streamline distributions at 98% span at U8 condition. In this figure, two radial vorticity concentrated regions are observed, the one near the pressure surface is a positive radial vorticity region and the other one near the suction surface is a negative radial vorticity region. In combination with the streamline distribution, it is clear that fluids near the pressure surface rotate counterclockwise because of the shearing action between the incoming flow and the reverse flow, therefore a positive radial vorticity concentrated region is formed. Similarly, fluids near the suction surface rotate clockwise, thus a negative radial vorticity concentrated region is formed. Besides, a stagnation point is also found upstream of the radial vorticity concentrated region. These characteristics mentioned above correspond to the features of vortex spiral-type breakdown proposed by Brücker and Althaus (1993), imply a spiral-type tip vortex breakdown occurs at this condition.

Further analyses of the flow field show that the evolution and development of the U-type vortex is cyclical. Figure 18 presents instantaneous flow structures and the C_p distribution on the pressure surface during one T_{ref} for U8. It is observed that the U-type vortex moves pitchwise to the adjacent blade after it is formed in the middle of the passage and finally impinges on the pressure surface at $t=0$,

then it gradually moves away from the leading edge of the pressure surface. The vortex development is periodical, and its periodic time turn out to be about 94τ since the flow field at $t=0$ is similar to that at $t=94$ especially in the vortex structure. The period of 94τ corresponds with the periodic time of the pressure fluctuation seen in Fig. 7. Besides, it should be noted that the U-type vortex sheds from the TLV at $t=40$, after that, it gradually moves away from the leading edge of the blade with its strength decaying and cannot maintain its U-type configuration. Combining the information shown in Figs. 12 and 13, the shedding of the U-type vortex can be explained as follows: at $t=40$, the blade loading reaches to a peak, and the recirculation region has a minimal volume. Accordingly, the shearing action between the reverse flow and the incoming main flow weakens, leading to a strength reduction of the U-type vortex. As a result, the U-type vortex cannot maintain its configuration and sheds from the TLV.

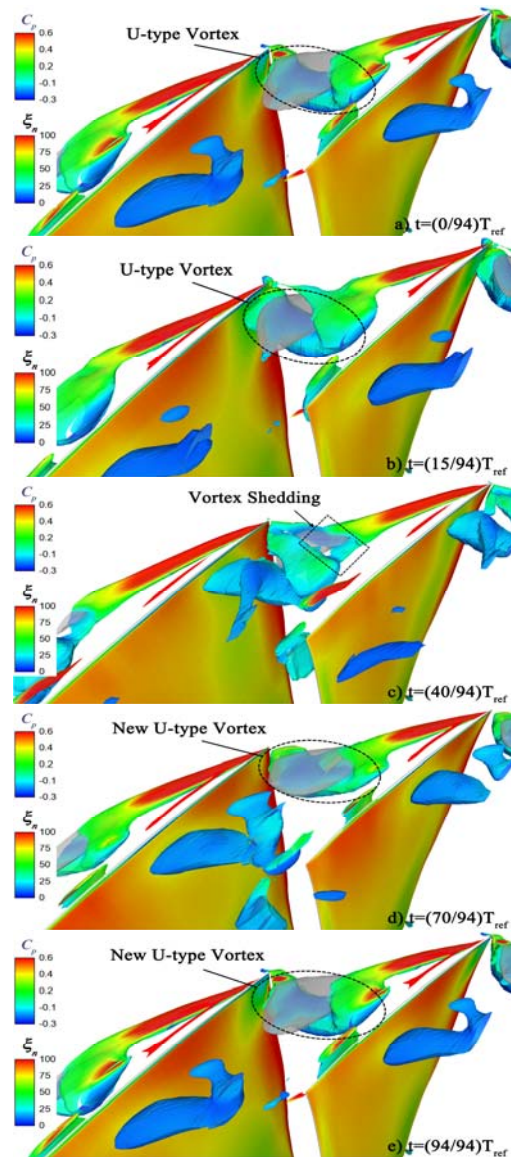
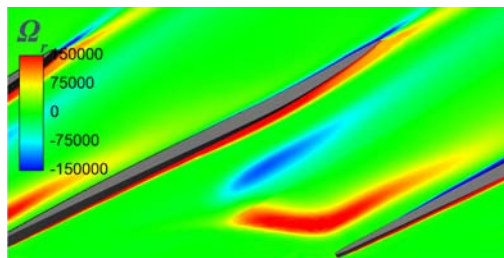
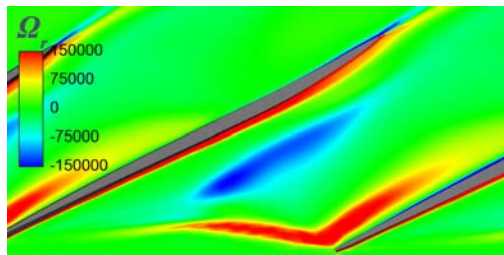


Fig.18. Instantaneous flow structures and the C_p distribution on the pressure surface during one T_{ref} for U8

Additionally, it is also found that the periodic development of the U-type vortex has a significant influence on the blade loading. The U-type vortex impinges on the adjacent blade, resulting in a large low pressure region on the pressure surface. Then the U-type vortex moves downstream, which enables the static pressure at the leading edge of the pressure surface recovers. At $t=40$, the blade loading reaches to a peak, meanwhile, the old U-type vortex sheds from the TLV. At $t=70$, a new U-type vortex is formed in the middle of the passage. Afterwards, it moves along pitchwise to the adjacent blade, which contributes to the pressure reduction at the leading edge of the pressure surface. The whole process mentioned above corresponds to the pressure oscillation shown in Fig. 8.



(a) U4 condition



(b) U5 condition

Fig. 19. Time-averaged radial vorticity and streamline distributions at 98% span at U4 and U5 conditions

Figure 19 provides the time-average radial vorticity and streamline distributions at 98% span at U4 and U5 conditions. Note that for operating condition approaching the stability limit, tip flow unsteadiness is first observed at U5. It is found that the TLV breakdown and the U-type vortex are observed at both conditions. However, the U-type vortex does not impinge on the pressure surface of the adjacent blade at U4 condition and has no effect on the blade loading. Thus, no massflow oscillation is detected at U4 condition. These analyses indicate that U-type vortex's impingement on the pressure surface of the blade is the direct cause of the blade loading variation.

5. CONCLUSIONS

In this paper, single-passage unsteady simulations have been conducted on NASA Rotor 35, and results are validated by experimental data. The trigger and origin of the flow unsteadiness in the blade passage is discussed in detail. The results are summarized as follows:

- (1) For operating condition approaching the stability limit, tip flow unsteadiness is observed at near stall conditions, and the main fluctuation region is confined within the fore 30% of tip chord above 94.2% span.
- (2) The TLV breakdown is not the decisive factor that leads to the flow unsteadiness because the TLV still breaks down in conditions that no flow unsteadiness is detected.
- (3) The TLV breaks down after interacting with the shock. Then a U-type vortex emerges from the shearing action between the incoming main flow and the reverse flow.
- (4) The mutual interference among the motion of the U-type vortex, the vibration of the blade loading and the volume of the recirculation region form a self-sustained system.
- (5) The vibration of the blade loading marks the beginning of an unsteadiness in the passage. And the U-type vortex's periodic impingement on the blade pressure surface is regarded as a trigger of the blade loading vibration.
- (6) The shock oscillation is not a cause of the flow unsteadiness, but a manifestation of the flow unsteadiness.

ACKNOWLEDGEMENTS

The authors would like to acknowledge the supports of National Natural Science Foundation of China, Grant No. 11572257, 51536006, 51790512 and the practical support of Natural Science Foundation of Shaanxi province, Granted No. 2017JM5055.

REFERENCES

- Adamczyk, J. J., M. L. Celestina, and E. M. Greitzer, (1993). The Role of Tip Clearance in High-Speed Fan Stall. *Journal of Turbomachinery* 115(1), 28-38.
- Brücker, C. (1993). Study of vortex breakdown by particle tracking velocimetry. Part 2: spiral-type vortex breakdown. *Experiments in Fluids*, 14(1), 133-139.
- Delery, J. M. (1994). Aspects of vortex breakdown. *Progress in Aerospace Sciences*, 30(1), 1-59.
- Deng, X. (2006). *Numerical Investigation into Tip Leakage Flow*. Ph. D. thesis, Graduate School of Chinese Academy of Sciences, Beijing, China.
- Du, J., F. Lin, H. Zhang, J. Chen (2008). Numerical Investigation on the Originating Mechanism of Unsteadiness in Tip Leakage Flow for a Transonic Fan Rotor. *ASME Turbo Expo 2008*, 323 (323), 147-154.
- Furukawa, M. (1999). The role of tip leakage vortex breakdown in compressor rotor aerodynamics, *Journal of turbomachinery* 121(3), 469-480.
- Furukawa, M., M. Kazuhisa, K. Yamada and M.

- Inoue (2000). Unsteady Flow Behavior due to Breakdown of Tip Leakage Vortex in an Axial Compressor Rotor at Near-Stall Condition. *ASME Turbo Expo 2000* No. 2000-GT-0666.
- Hah, C., C. D. Rabe, and R. A. Wadia (2004). Role of Tip-Leakage Vortices and Passage Shock in Stall inception in a swept transonic compressor rotor. *ASME Turbo Expo 2004* No. GT2004-53867.
- Hah, C., J. Bergner and H. P. Schiffer (2006). Short Length-Scale Rotating Stall Inception in a Transonic Axial Compressor: Criteria and Mechanisms. *ASME Turbo Expo 2006* No. GT2006-90045.
- Inoue, M. and M. Kuromaru (1989). Structure of Tip Clearance Flow in an Isolated Axial Compressor Rotor. *Journal of Turbomachinery* 111(3), 250-256.
- Inoue, M., M. Kuromaru, and M. Fukuhara (1986). Behavior of Tip Leakage Flow Behind an Axial Compressor Rotor. *Journal of Engineering for Gas Turbines and Power* 108(1), 7-14.
- Jameson, A. (1991). Time dependent calculations using multigrid, with applications to unsteady flows past airfoils and wings. *Computational Fluid Dynamics Conference*.
- Leibovich, S. (2003). The structure of vortex breakdown. *Annual Review of Fluid Mechanics* 10(10), 221-246.
- Reid, L. and R. D. Moore (1978). Design and overall performance of four highly loaded, high speed inlet stages for an advanced high-pressure-ratio core compressor. *NASA Tp-1337*
- Sarpkaya, T. (1971). On stationary and travelling vortex breakdowns. *Journal of Fluid Mechanics*, 45(3), 545-559.
- Van Zante, D. E., Strazisar, A. J., Jerry, R., Hathaway, M. D and Okiishi, T. H. (2000). Recommendations for Achieving Accurate Numerical Simulation of Tip Clearance Flows in Transonic Compressor Rotors. *Journal of Turbomachinery* 122 (4) :733-742
- Wu, Y., G. An, Z. Chen and W. Peng (2016). Numerical investigation into unsteady flow and its associated flow mechanism in a transonic compressor rotor at near stall conditions. *Journal of Propulsion Technology* 37(10), 1847-1854
- Wu, Y., Q. Li, J. Tian and W. Chu (2012). Investigation of Pre-Stall Behavior in an Axial Compressor Rotor—Part I: Unsteadiness of Tip Clearance Flow. *Journal of Turbomachinery* 134(5):051027.
- Wu, Y., Q. Li, W. Chu, H. Zhang and Z. Su (2010). Numerical investigation of the unsteady behaviour of tip clearance flow and its possible link to stall inception. *Proceedings of the Institution of Mechanical Engineers, Part A: Journal of Power and Energy* 224(1):85-96.
- Yamada, K., M. Furukawa, T. Nakano, M. Inoue and K. Funazaki (2004). Unsteady Three-Dimensional Flow Phenomena Due to Breakdown of Tip Leakage Vortex in a Transonic Axial Compressor Rotor. *ASME Turbo Expo 2004* No. GT2004-53745.